Journal of Advanced Ceramics https://mc03.manuscriptcentral.com/jacer
J Adv Ceram 2025, **14**: 9221170

https://doi.org/10.26599/JAC.2025.9221170

Research Article

Stabilization mechanism of antiferroelectric *Pnma* phase and low-field reversible phase transition in sodium niobate-based ceramics

Min Chen[1,✉], Lei Zhang[2,✉], Yongping Pu[2,✉], Fangping Zhuo[3], Jing Shang[2], Yu Shi[2], Hongliang Du[1]

[1] *Multifunctional Electronic Ceramics Laboratory, College of Engineering, Xi'an International University, Xi'an 710077, China.*

[2] *School of Materials Science and Engineering, Shaanxi Key Laboratory of Green Preparation and Functionalization for Inorganic Materials, Shaanxi University of Science and Technology, Xi'an 710021, China.*

[3] *Department of Materials and Earth Sciences, Technical University of Darmstadt, Darmstadt 64287, Germany.*

✉ Corresponding authors.

E-mail: M. Chen, cmsociety@163.com;

L. Zhang, zlsociety@163.com;

Y. Pu, puyongping@sust.edu.cn

Received: June 4, 2025; Revised: August 8, 2025; Accepted: September 7, 2025

Abstract: The stabilization mechanism of antiferroelectric (AFE) phases in sodium niobate ceramics remains unclear, leading to irreversible AFE–ferroelectric (FE) phase transitions and requiring a high operating E-field, which significantly limits the utilization of AFE properties. In this work, leveraging insights from density functional theory calculations, we design and fabricate $x$$Bi_{2/3}SnO_3$-(1-$x$)$NaNbO_3$ ceramics, overcoming these limitations by achieving both a reversible AFE–FE phase transition and a low operating field (< 200 kV·cm^{-1}). Notably, the optimized composition exhibits an exceptionally low remanent polarization compared to conventional AFE systems. Structural analysis reveals a three-stage phase evolution with increasing x: FE Q + AFE P phases (x < 0.02) →pure AFE P phase (x = 0.02) →coexistence of AFE P + AFE R phases (0.02 < x < 0.08). The AFE P phase is characterized by a 4-layer multicell structure (~1.65 nm), periodically disrupted by 6-layer antiphase boundaries (APBs, ~2.44 nm), which are associated with dislocation formation and a large energy difference between P and Q phases (7.20 meV·f.u.$^{-1}$). These features likely contribute to reduced domain size and lower field-induced AFE→FE transition. Furthermore, the stabilization of the AFE R phase is primarily caused by a reduction in the distortion index (from 0.047 to 0.003) and enhanced covalency in A-O and B-O bonds. This study provides new insights and theoretical guidance for developing low-field-driven reversible phase transitions in AFEs.

Keywords: antiferroelectrics, low-field, phase transition, sodium niobate

1 Introduction

Antiferroelectric (AFE) materials undergo complex yet reversible phase transitions between AFE and ferroelectric (FE) states under applied external E-fields, enabling their applications in IR pyroelectric detectors[1, 2], explosive-to-electrical transducers[3], high energy storage capacitors[4-7], digital displacement transducers[8-10], large-strain actuators[11], electrocaloric cooling devices[12, 13], non-volatile random access memories[14, 15], etc. Driven by the search for high performance, environmental

friendliness, and low cost, sodium niobate ($NaNbO_3$; NN), a well-established AFE material, has recently attracted significant research interest[15-21]. However, in pure NN ceramics, the AFE P (*Pbcm*, Glazer tilt system: $a^-a^-b^+/a^-a^-b^-$[22, 23]) and FE Q ($Pmc2_1$, Glazer tilt system: $a^-a^-b^+$) phase have a minimal energy difference[15, 24, 25], leading to irreversible field-induced phase transitions and the absence of double polarization loops.

Early reports on stabilizing the AFE phase in NN have shown promising progress, but achieving fully reversible double hysteresis loops remains a significant challenge. Several end-members, such as $CaHfO_3$[26], $CaSnO_3$[27], and $SrSnO_3$[15], have been found to induce double loops at room temperature (RT). However, most NN-based ceramics with double polarization loops exhibit negative backward critical fields ($E_{FE\text{-}AFE} < 0$), meaning the field-induced FE phase does not fully revert to the AFE state upon removing the E-field, resulting in a large remanent polarization (P_r) —a phenomenon known as partially reversible phase transition. Currently, only a few NN-based ceramics exhibit a completely reversible field-induced phase transition ($E_{FE\text{-}AFE} > 0$) at RT. However, these materials require E-fields exceeding 200 kV·cm^{-1} to trigger the AFE–FE phase transition, which limits their potential applications in large-scale integrated circuits and low-voltage electronics. Therefore, developing novel NN-based AFE systems and uncovering the underlying mechanisms governing low-field reversible AFE–FE phase transitions is of great significance. Additionally, the high-temperature AFE R phase (*Pnma*, Glazer tilt system: $a^-b^+c^+/\ a^-b^+c^+/a^-b^0c^+$[28, 29]) has been observed in NN-based ceramics exhibiting double polarization loops[16, 25, 30-34], but its stabilization mechanism remains unclear.

In this work, guided by density functional theory (DFT) calculations, we design and fabricate $x$$Bi_{2/3}SnO_3$-(1-$x$)$NaNbO_3$ ceramics, overcoming the long-standing challenges of achieving both a fully reversible field-induced phase transition ($E_{FE\text{-}AFE} > 0$) and a low operating field ($E_{AFE\text{-}FE} < 200$ kV·cm^{-1}). Compared to other Bi-based modifiers ($BiMg_{2/3}Ta_{1/3}O_3$, $BiHfO_3$, and $BiScO_3$), $Bi_{2/3}SnO_3$ enables simultaneous enhancement of polarization and energy efficiency through synergistic mechanisms: stereochemically active Bi^{3+} $6s^2$ lone-pair orbital hybridization combined with Sn^{4+}-induced relaxor

behavior[35, 36]. Furthermore, we reveal the stabilization mechanism of the AFE R phase and the low-field reversible phase transition from the atomic to the phase scale, providing valuable insights into the future development of high-performance AFE ceramics.

2 Experimental

2. 1 Ceramic preparation

$x$$Bi_{2/3}SnO_3$-(1-$x$)$NaNbO_3$ ceramics (x=0.00~0.08) were synthesized via solid state reaction. Raw materials included analytically pure Na_2CO_3 (99.80%), Nb_2O_5 (99.50%), Bi_2O_3 (99.00%), and SnO_2 (99.50%) (Sinopharm, China) powders, weighed following the stoichiometric ratio, and then ball-mixed in ethanol for 10 h. After ball milling, the obtained slurries were dried and placed in a dryer at 80 °C for a day, and then pressed into cylindrical shapes. The shaped powders were calcined at a heating rate of 5 °C/min to 800 °C, held for 3 h, then ball milled again for 4 h. Afterwards, disc-shaped samples were prepared by manual pre-pressing followed by cold isostatic pressing at 200 MPa. Finally, sintering was conducted in sealed crucibles with composition-matched sacrificial powder, using a heating rate of 2 °C/min to optimize temperatures (x=0.00: 1330°C, x=0.02: 1320°C, x=0.04: 1270°C, x=0.06: 1240°C, x=0.08: 1230°C) with a 3-hour dwell time at each peak temperature.

2. 2 Characterization methods

The X-ray diffraction (Smart Lab 9kW, Rigaku company, Tokyo, Japan), Raman spectroscopy (Renishaw, Renishaw-invia, UK), and transmission electron microscope (TEM, Tecnai G2 F30, FEI, USA) were employed to identify the P, Q, and R phases in NN-based ceramics. The TEM specimens were prepared using the FIB system of FEI Helios G4 platform. Prior to scanning electron microscopy (SEM, Apreo S, FEI, USA) imaging, polished ceramic samples were thermally etched at 1200°C for 30 minutes to delineate grain boundaries. Representative micrographs (Fig. S1) confirm >96% relative density and a grain size range of 2.08~4.16 μm. Ferroelectric and dielectric tests (temperature-dependent permittivity and impedance spectroscopy measurement) were carried out using a

ferroelectric analyzer (Aixacct, TF2000E, Germany) and an LCR meter (Agilent, E4980A, USA). For ferroelectric measurements, samples (diameter ≈10 mm) were polished to a thickness of 0.13 mm and electroded with 3-mm-diameter silver electrodes.

2. 3 Calculation methods

The DFT simulations have been performed using the Vienna Ab initio simulation (VASP)[37] package, implemented within the Perdew-Burke-Ernzerhof (PBE) function[38] and generalized gradient approximation (GGA)[39] for the geometry optimizations and the energy calculations of both pure and doped $NaNbO_3$ systems with AFE and FE phases. The AFE and FE phases were modeled using the *Pbcm* and *Pmc2₁* space groups, respectively. A supercell structure consisting of 80 atoms was employed for all calculations. The convergence criteria for the residual forces and total energy were set to 10^{-2} eV·Å^{-1} and 10^{-4} eV, respectively, with a plane-wave energy cutoff of 450 eV. The Brillouin zone was represented by Monkhorst-Pack special k-point meshes [40] of 4 × 9 × 3 for AFE phase structures and 3 × 9 × 4 for FE phase, respectively. The energy difference (ΔE) between the AFE and FE phases was calculated as $\Delta E = (E_{AFE} - E_{FE})/16$, where E_{AFE} and E_{FE} represent the total energies of the AFE and FE phases, respectively.

3 Results and discussion

Figs. 1(a-d) present the *P-E* loops and *I-E* curves for $x$$Bi_{2/3}SnO_3$-(1-$x$)$NaNbO_3$ ceramics. In pure NN ceramics, due to the irreversible field-induced phase transition, the *P-E* loop and *I-E* curve exhibit FE-like characteristics[25, 41-43]. However, when the $Bi_{2/3}SnO_3$ content reaches $x \geq 0.04$, the samples display typical AFE double *P-E* loops, characterized by four distinct current peaks in the corresponding *I-E* curves. The two peaks at higher fields correspond to the forward critical field $E_{AFE\text{-}FE}$, where the initial state transitions to the FE state. The two peaks at lower fields are associated with the backward critical field $E_{FE\text{-}AFE}$, where the FE state reverts to the AFE state. Our observed increase in both $E_{AFE\text{-}FE}$ and $E_{FE\text{-}AFE}$ with increasing doping levels suggests an enhanced stability of the AFE phase. The permittivity

stability against the applied field is very important for DC-link capacitor applications. The field-dependent permittivity can be easily calculated from dP/dE. Fig. 1(e) illustrates the E-field dependence of the calculated permittivity ε_{cal} for these ceramics. In pure NN, ε_{cal} decreases rapidly with increasing E-field, limiting its potential application in pulse power systems. In contrast, for compositions with $x \geq 0.02$, ε_{cal} increases with the applied E-field ($< E_{AFE\text{-}FE}$). The gradually gentler increase of the ε_{cal} below $E_{AFE\text{-}FE}$ with increasing x should be attributed to the mild AFE-FE phase transition enabled by enhanced relaxation behavior. Fig. 1(f) compares the $E_{AFE\text{-}FE}$, $E_{FE\text{-}AFE}$, and P_r across various $NaNbO_3$-based ceramics that exhibit double hysteresis loops at RT. Notably, for $0.04 \leq x \leq 0.08$, the ceramics demonstrate reversible field-induced phase transitions ($E_{FE\text{-}AFE} > 0$) with $E_{AFE\text{-}FE}$ below 200 kV·cm^{-1}. Compared to other NN-based AFE ceramics, $x Bi_{2/3}SnO_3$-(1-x)$NaNbO_3$ ceramics exhibit superior potential for integration into large-scale and low-voltage circuits, making them promising candidates for future electronic applications.

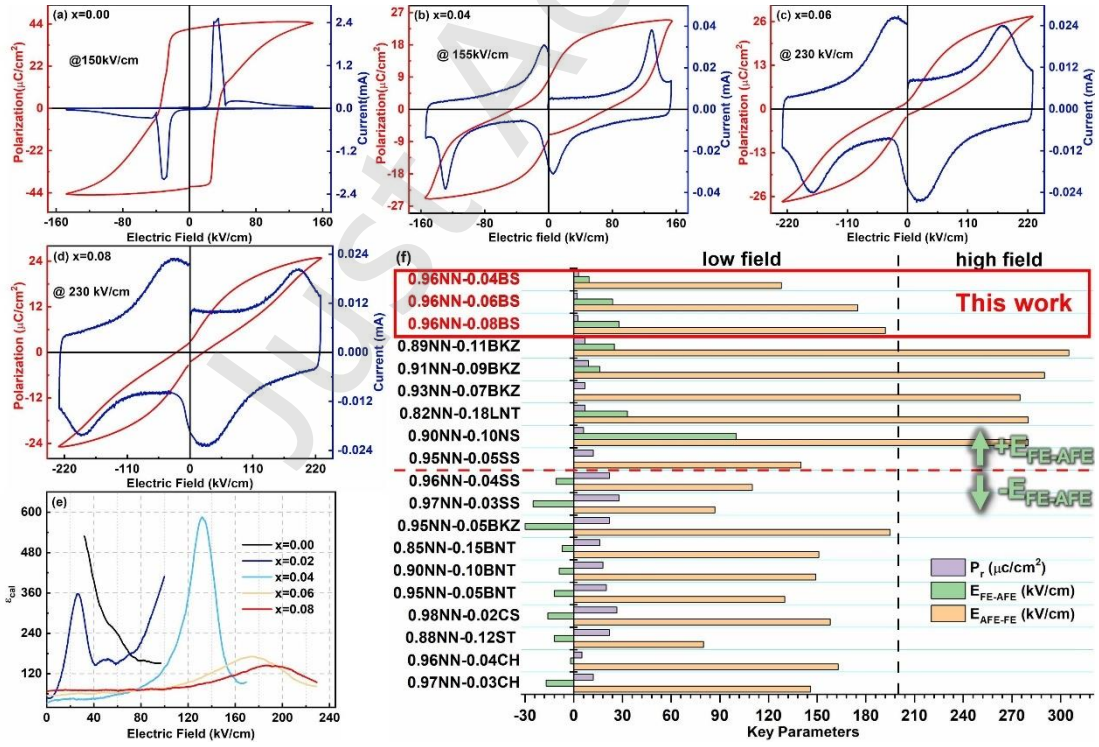

Fig. 1 (a-d) *P-E* loops with corresponding *I-E* curves at 10 Hz, and (e) ε_{cal} for $x$$Bi_{2/3}SnO_3$-(1-$x$)$NaNbO_3$ ceramics, (f) comparison of $E_{AFE\text{-}FE}$, $E_{FE\text{-}AFE}$, and P_r of $NaNbO_3$-based ceramic system that exhibit double *P-E* loops at RT[15, 16, 26, 27, 31, 44-46].

All $x$$Bi_{2/3}SnO_3$-(1-$x$)$NaNbO_3$ ceramics show the perovskite structure without noticeable second phases, as confirmed by XRD analysis (Fig. 2(a)). To gain deeper insight into the AFE phase, high-resolution XRD (HR-XRD) measurements were conducted, focusing on specific 2θ=35.1-37.8° (Fig. 2(b)), 33.5-34.5° (Fig. 2(c)), and 53.5-56.5° (Fig. 2(d)). The presence of the AFE P phase is evident across all ceramic samples, as indicated by the characteristic ¼ type superlattice diffraction peaks. Furthermore, a ⅙ type superlattice diffraction peak appears in the x=0.04 sample and becomes more pronounced with increasing $Bi_{2/3}SnO_3$ content, suggesting the progressive stabilization of the AFE R (*Pnma*) phase at RT[25, 47]. Additionally, the gradual shift of superlattice peaks toward higher angles indicates a contraction of the unit cell, primarily due to the substitution of larger Na^+ ions (r = 1.39 Å, CN=12) at A-sites by smaller Bi^{3+} ions (r = 1.36 Å, CN=12), with additional contribution from A-site vacancies of the end-member.

Raman spectroscopy is sensitive to the local ionic configuration, and shows an obvious difference in active modes to distinguish the P, Q, and R phases in NN-based ceramics. Fig. 2(e) presents the Raman spectra of the synthesized ceramics. Similar to pure $NaNbO_3$, all samples present eight vibrational modes within the measured range, corresponding to NbO_6 rotation, ν_6, ν_5, ν_4, ν_2, ν_1, ν_3, and $\nu_5 + \nu_1$, confirming their orthorhombic structure [48, 49]. According to the group theory, there are 60 Raman active modes in APE P phase expressed as $15A_g + 17B_{1g} + 15B_{2g} + 13B_{3g}$[50], the FE Q phase has 57 Raman active modes denoted by $16A_1 + 13A_2 + 12B_1 + 16B_2$[51], and the Raman active modes in APE R phase are described by $8A_g + 5B_{1g} + 7B_{2g} + 10B_{3g}$[52]. Nevertheless, there are only 14 modes that can be observed after using Lorentzian function deconvolution (see Fig.2(f)). The multi-peaks below 300 cm^{-1} represent a characteristic vibrational fingerprint of the antiferroelectric P-phase, arising

from large Nb-O bond length disparities induced by antiparallel Nb. Composition-dependent shifts of these Raman bands are plotted in Fig. 2(g). When $x \leq 0.02$, most vibrational modes shift to lower wavenumbers while retaining the total number of active modes. This behavior aligns with the previously observed transition from a coexisting FE Q + AFE P (Q + P) phase to a pure AFE P phase in the $(Li_xNa_{1-x})NbO_3$ solid solution[51]. Concurrently, these spectral changes indicate the decrease inn the difference between the B-O bond length within the lattice, leading to the improvement of electron localization[16]. With further addition of $Bi_{2/3}SnO_3$, certain Raman modes—particularly those near 150, 200, and 700 cm^{-1} wavenumbers —disappear, while the remaining modes remain nearly unchanged for $x \geq 0.04$. This observation is in accordance with previous reports about $NaNbO_3$ ceramics, where the R phase emerges upon heating[53]. Fig. 2(h) presents the full-width at half-maximum (FWHM) variations for selected Raman modes. As x increases, the FWHM of ν_1 broadens, while that of ν_5 remains relatively constant for $x \geq 0.04$. These trends correlate well with the observed structural phase transitions. The increase in FWHM reflects the enhancement of relaxation behavior because of local structural disorder. In summary, the sample undergoes three stages of phase transition with increasing doping content: Q + P phases ($x < 0.02$) →pure P phase ($x = 0.02$) →coexistence of P and R (P + R) phases ($0.02 < x < 0.08$).

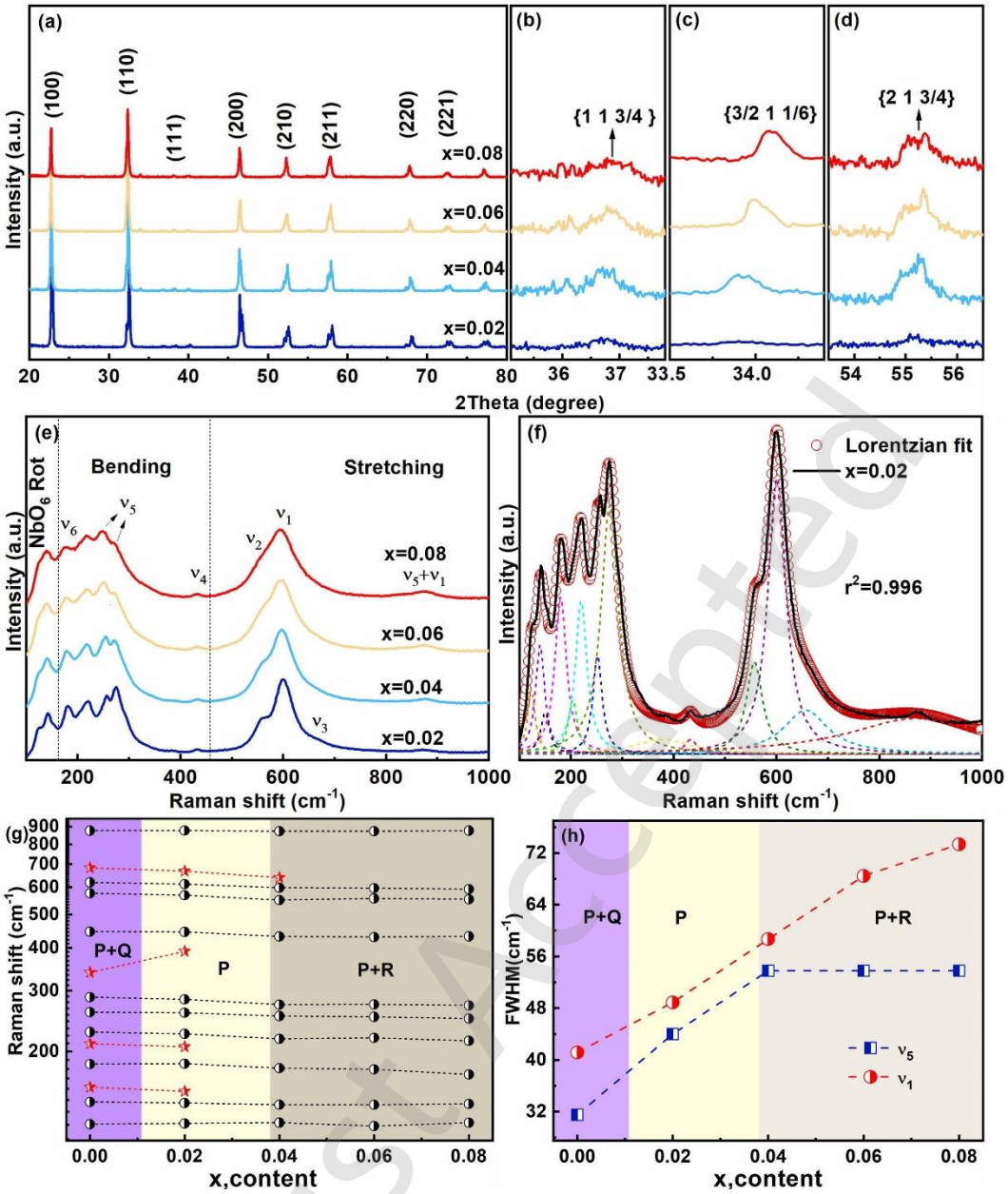

Fig.2(a) XRD patterns for xBi$_{2/3}$SnO$_3$-(1-x)NaNbO$_3$ ceramics; the close inspection about (b) {1 1 3/4}, (c) {1 1 3/4} and (d) {2 1 3/4} superlattice peaks by high resolution XRD; (e) Raman shift; (f) multi-peak fitting based on Lorentz area function; (g) wavenumber versus compositions after fitting; (h) the FWHM of v_1 and v_5 modes.

It is generally accepted that NN undergoes the following major polymorphic phase transitions accompanied by dielectric anomalies upon heating[33, 54]:

$$\text{FE N (Rhombohedral)} \xrightarrow{\sim -100^{\circ}\text{C}} \text{AFE P (Orthorhombic)} \xrightarrow{\sim 360^{\circ}\text{C}} \text{AFE R (Orthorhombic)} \xrightarrow{\sim 480^{\circ}\text{C}} \text{PE} \quad .$$

Similar to pure NN, $Bi_{2/3}SnO_3$ modified NN ceramics also exhibit these anomalies in their dielectric diagram, as manifested in Figs. 3(a-c). The permittivity ε increases gradually at RT, mainly attributed to the increase of the dielectric peak at $T_{N\text{-}P}$ (phase transition temperature of the N→P). At the same time, the shift of $T_{P\text{-}R}$ (phase transition temperature of the P→R) towards RT indicates that the AFE R phase is gradually stabilized. According to the analysis above, Fig. 3(d) summarizes the phase diagram of the $NaNbO_3$-$Bi_{2/3}SnO_3$ binary system. With the introduction of $Bi_{2/3}SnO_3$, almost all phase transition temperatures move to lower temperatures, while transitions from FE N phase to AFE P phase ($T_{N\text{-}P}$) show the opposite trend. Similar phenomena have been observed in the BMT modified NN and (1-x)$NaNbO_3$-$x$$CaZrO_3$ system[33, 55]. As reported in other NN-based ceramics featured double hysteresis loops[15, 24, 26, 27, 32], $T_{P\text{-}R}$ drops approximately linearly, indicating that high-temperature R phase gradually stabilizes at RT. With the increase of doping amount, the $T_{R\text{-}P}$ obtained by the cooling curve of dielectric permittivity[56] (Fig. S2) drops sharply below RT, resulting in a broader phase coexistence region between the R and P phases. This means the stability of the AFE phase at RT. Therefore, the ceramic system experiences these three stages by adding $Bi_{2/3}SnO_3$:

(1) Q + P phases with FE characteristic *P*-*E* loops ($x < 0.02$);

(2) the single P phase with double *P*-*E* loops accompanied by a negative $E_{EF\text{-}AFE}$ ($x = 0.02$);

(3) the P + R phases with well-developed double *P*-*E* loops ($0.02 < x < 0.08$).

It is worth mentioning that our method for determining $T_{R\text{-}P}$ can also account for the recent observation of double hysteresis loops in NN at 320 °C, as reported by Zuo et al.[45]. However, it is regrettable that $T_{Q\text{-}P}$ and $T_{P\text{-}Q}$ are absent from the phase diagram due to current technological limitations. Despite this, the proposed phase diagram serves as a valuable framework for guiding the exploration of NN-based AFE materials. Future refinements, incorporating higher-resolution techniques, will further enhance its accuracy and comprehensiveness.

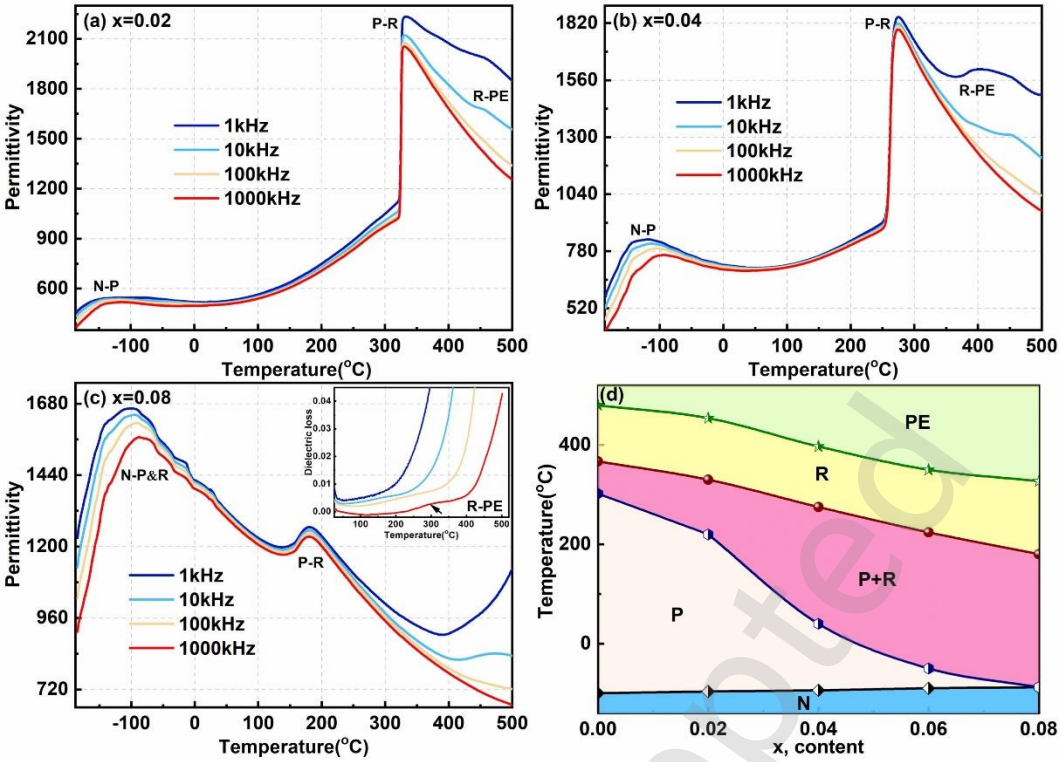

Fig. 3(a-c) Temperature-dependent permittivity, and (d) phase diagram for the $NaNbO_3$-$Bi_{2/3}SnO_3$ binary system.

The dielectric peaks (~-100 °C) in all samples shift to higher temperatures, and their corresponding permittivities decrease with the frequency increases. The frequency dispersion and broadened dielectric peaks indicate the relaxation behavior of the sample by incorporating ions (Bi^{3+} and Sn^{4+}) of different valence states and sizes to A/B sites, which coincides with the analysis in Raman. The modified Curie-Weiss law with dispersion index γ and Curie constant C is employed to further explore the relaxation behavior[57]:

$$\frac{1}{\varepsilon}-\frac{1}{\varepsilon_{\mathrm{m}}}=\frac{(T-T_m)^{\gamma}}{C} \quad (1),$$

here, T_{m} denotes the temperature corresponding to the maximum permittivity ε_{m}. It is found that γ increases with the addition of $Bi_{2/3}SnO_3$ via linearly fitting the plots of ln ($1/\varepsilon$-$1/\varepsilon_{\mathrm{m}}$) versus ln ($T$-$T_{\mathrm{m}}$), as displayed in Fig.4(a). The increased γ indicates that the relaxation behavior of the sample is enhanced[58]. The enhanced relaxation behavior in AFEs leads to a mild AFE-FE phase transition and

low energy dissipation, preventing the breakdown caused by drastic structural deformation observed in normal FEs, thereby facilitating the realization of double hysteresis loops[59]. The impedance spectroscopy (Fig.4(b)) is employed at 600 ºC to investigate the conduction mechanism. The single nearly semicircular arc presented in the Z'–-Z'' plots at 600 ºC implies that a single relaxation mechanism is dominant in the studied system[60]. All these semicircular arcs can be fitted well by a group of parallel R‖CPE (CPE is the constant phase element) equivalent circuit model in Fig.4(b). The conductivity in dielectric ceramics is related to thermal activation, and the activation energy E_a can be given by the Arrhenius law with the pre-exponent constant σ_0, the bulk conductivity ($\sigma = \frac{H}{RS}$) and the Boltzmann constant k[61, 62]:

$$\sigma = \sigma_0 \exp\left(-\frac{E_a}{kT}\right) \quad (2).$$

Therefore, E_a can be obtained by linear fitting the lnσ–1000/T plots (inset of Fig. 4(c)) and is summarized in Fig. 4(c). The E_a in this system is within the range of 0.77–1.19 eV and increases with the addition of $Bi_{2/3}SnO_3$. Generally, the E_a of oxygen vacancies ranges from 0.5 eV to 2 eV[62]. The increased E_a probably means that charge carriers (such as oxygen vacancies) must overcome a larger energy barrier to participate in conductance, thereby contributing to the improved breakdown strength E_b. Fig.4(d) shows the E-field dependent leakage current density (LCD) for $x$$Bi_{2/3}SnO_3$-(1-$x$)$NaNbO_3$ system. The LCD of the doped samples is almost the same and much lower than that of pure NN. The characteristically high leakage current and low breakdown strength of pure $NaNbO_3$ ceramics typically originate from thermally generated defects like oxygen and sodium vacancies, formed during high-temperature sintering. The reduced leakage current observed after $Bi_{2/3}SnO_3$ addition demonstrates that the related vacancy concentration was effectively reduced, primarily through the substitution of Na^+ by Bi^{3+}. Furthermore, as discussed above, $Bi_{2/3}SnO_3$ addition enhances electron localization, which is also favorable for the enhancement of E_b.

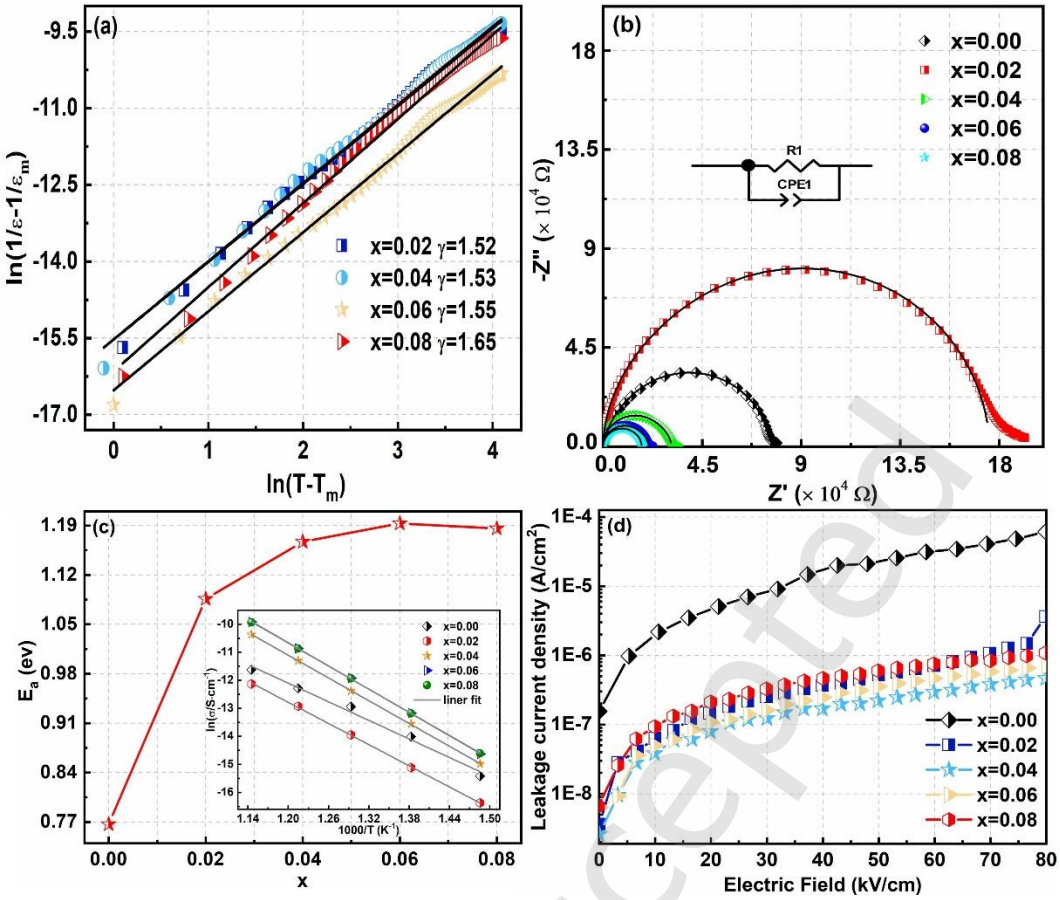

Fig. 4(a) The ln (T - T_m) –ln ($1/\varepsilon$-$1/\varepsilon_m$) plots at 1000 kHz, (b) the Z'–-Z'' plots and resistance fitting at 600 °C, (c) the summary of activation energy (the inset is Arrhenius plots), and (d) leakage current density for $x$$Bi_{2/3}SnO_3$-(1-$x$)$NaNbO_3$ ceramics.

The presence of the AFE P phase was further confirmed through selected area electron diffraction (SAED) patterns, which exhibit quarter-integer diffraction spots[63, 64] (indicated by white arrows in Fig. 5(a)). However, no distinct domains were observed in the bright-field TEM images (Fig. S3). To gain further insight into the domain structure, high-resolution TEM (HRTEM) was employed, and the corresponding original image is shown in Fig. 5(b). The periodically arranged 4-layer multicell structure, characteristic of the AFE P phase, is disrupted by a 6-layer antiphase boundary (APB)—a feature also observed in pure $NaNbO_3$ (NN) ceramics[33, 65]. The modulation widths of these two structures, determined from the intensity profile (in the bottom inset of Fig. 5(b)), measure approximately 1.65 nm and 2.44 nm, respectively. Interestingly, several dislocations are present in the

modified NN samples (Fig. 5(c)), further disrupting the lattice periodicity. $NaNbO_3$ As a result, this sample exhibits a significantly lower $E_{AFE\text{-}FE}$ compared to other reported NN-based AFE ceramics, such as (1-*x*)NN-*x*BKZ[44] and $(Na_{0.91}La_{0.09})(Nb_{0.82}Ti_{0.18})O_3$[46] ceramics. The reduced AFE→FE phase transition temperature is further verified through the cooling curve of the dielectric permittivity (Fig. S2). Furthermore, dislocations can pin domain walls, restricting their motion[66-69], which likely contributes to the formation of nanodomains observed in Fig. 5(d). These randomly distributed nanodomains should contribute to the relaxor behavior observed in Raman and dielectric results.

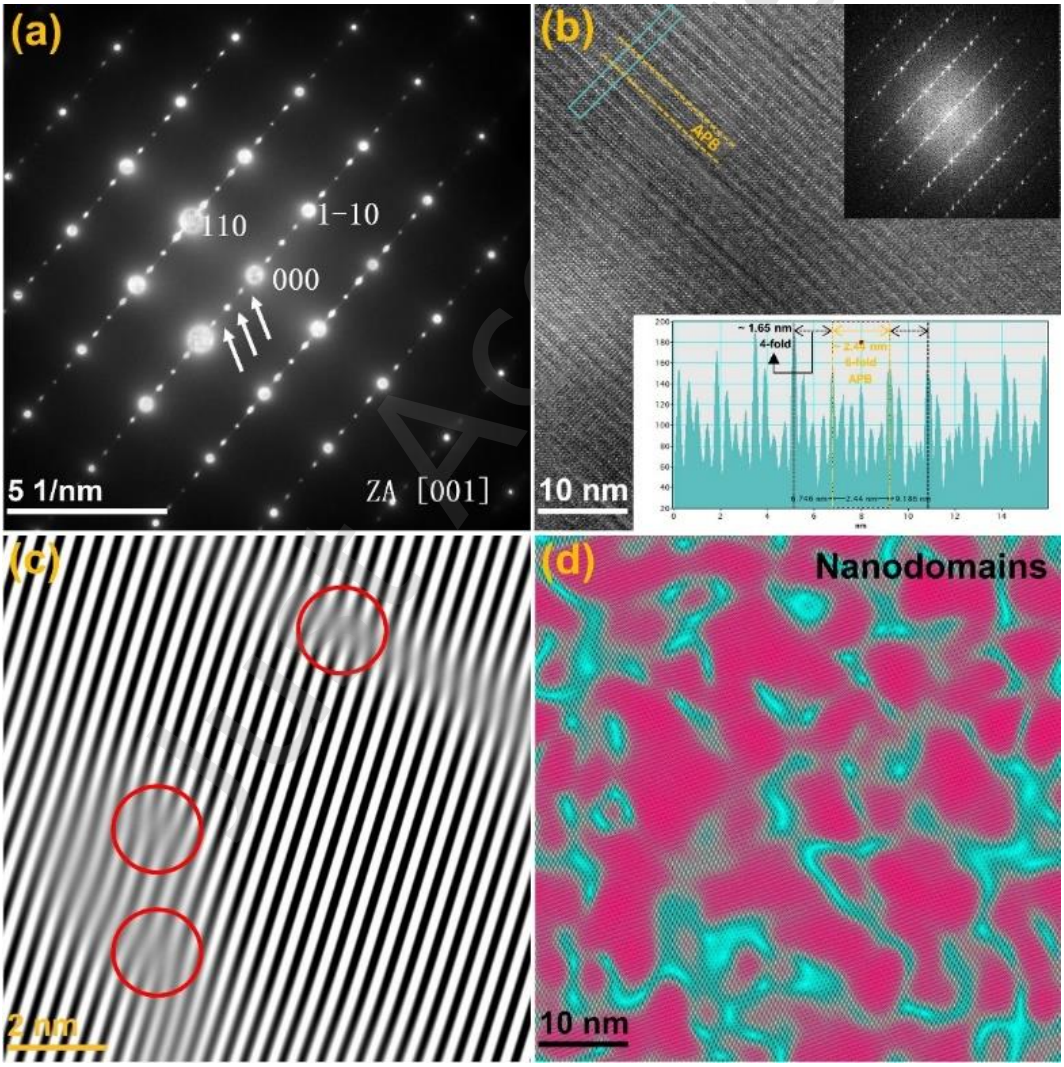

Fig. 5(a) SAED patterns along the [001] zone axis in the *x*=0.08 sample with white arrows marking the ¼ superlattice reflections. (b) The original HRTEM images with FFT analysis (top inset) and

intensity profile of the selected light blue box (bottom inset). (c) The IFFT pattern of the HRTEM image via masking ¼ type reflections in the corresponding FFT image, presenting dislocations marked by red circles. (d) Nanodomains obtained by IFFT images.

DFT calculations were performed to evaluate the free energy changes and the effect of $Bi_{2/3}SnO_3$ incorporation on the reversibility of the field-induced phase transition, as shown in Figs. 6(a-b). The results indicate that after introducing $Bi_{2/3}SnO_3$, the AFE P phase exhibits a lower free energy than the FE Q phase, with the energy difference increasing from 3.35 meV·f.u.$^{-1}$ to 7.20 meV·f.u.$^{-1}$. This larger energy gap enhances the stability of the AFE P phase, allowing the field-induced FE Q phase to more easily revert to the AFE P phase upon the removal of the E-field. To further explore the electronic structure, crystal structure analysis and Electron Localization Function (ELF) calculations were conducted (see Figs. 6(c-f) and Fig. S4). The ELF values range from 0 (blue) to 1 (red), where a higher ELF value indicates a higher degree of electron localization[70]. In polyatomic systems, regions with covalent bonding and lone pair electrons generally exhibit high electron localization[71, 72]. Figs. S4(c)-(d) present the ELF maps along the A-site atomic plane for pure NN and $0.08Bi_{2/3}SnO_3$-$0.92NaNbO_3$ ceramics, respectively. In pure NN, no electron localization (blue) is observed around Na atoms, indicating the typical ionic bonding nature of Na-O bonds. In contrast, for $0.08Bi_{2/3}SnO_3$-$0.92NaNbO_3$, a localized electron distribution (ELF > 0, light blue) appears around Bi-O bonds, suggesting an increase in covalency of A-O bonds. Similarly, ELF maps along the B-site atomic plane (Figs. 6(e)-(f)) show that oxygen atoms in pure NN are surrounded by a multi-layered confocal ellipsoidal shell electron localization distribution. After modification, the strongly localized electron regions (orange-red) shift noticeably towards Sn atoms, indicating an enhancement in the covalency of B-O bonds. The observed increase in covalency of both A-O and B-O bonds contributes to the improvement of E_b, which is crucial for maintaining double *P*-*E* loops at RT.

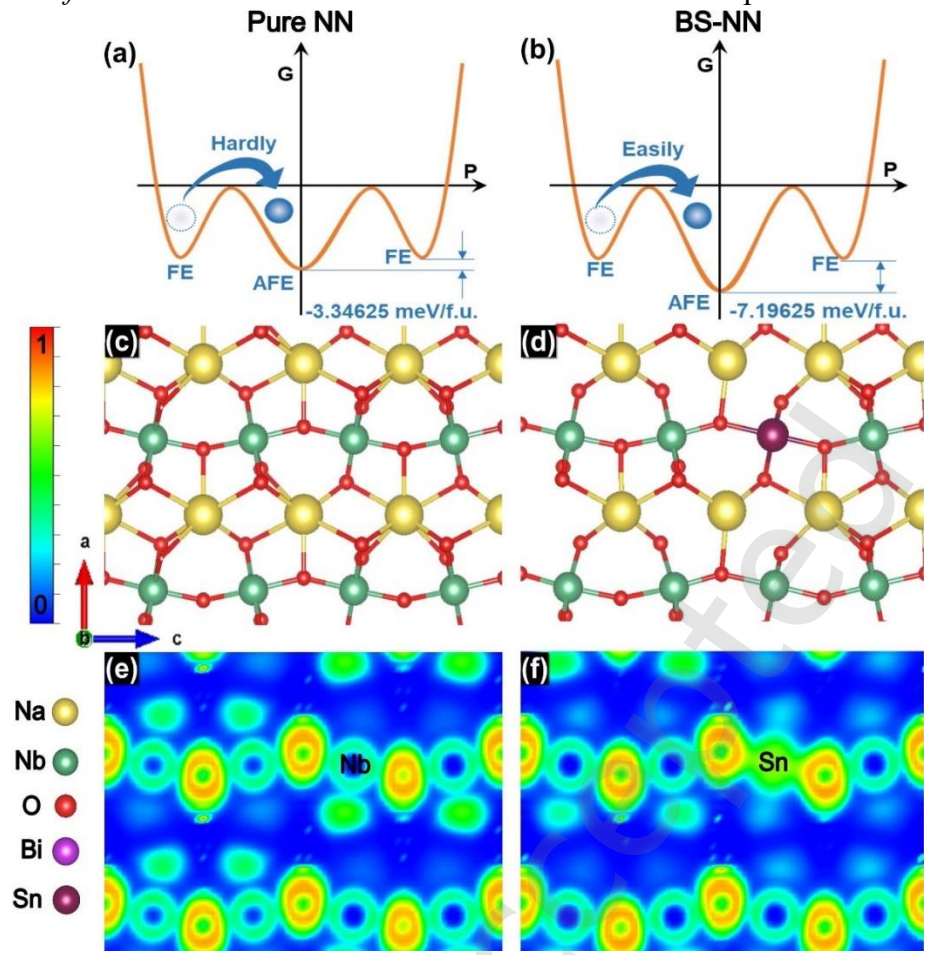

Fig. 6 Calculated energy results for (a) pure NN ceramic and (b) $0.08Bi_{2/3}SnO_3$-$0.92NaNbO_3$ ceramic; calculated crystal structures along the (c) Nb atomic plane in pure NN ceramic and (d) Sn atomic plane in $0.08Bi_{2/3}SnO_3$-$0.92NaNbO_3$ ceramic; the corresponding Electron Localization Function (ELF) maps in (e) pure NN ceramic and (f) $0.08Bi_{2/3}SnO_3$-$0.92NaNbO_3$ ceramic.

The displacements of B-site ions in the AFE R phase are relatively small[22]. In ABO_3-type perovskites, the extent of cation displacement typically increases during the cooling process[73]. To qualitatively evaluate the cation displacement in modified NN, the distortion index (D) of the [BO_6] octahedron based on Baur's polyhedral distortion theory is introduced as[74]:

$$D = \frac{1}{6}\sum_{i=1}^{6}\frac{|l_i - l_{av}|}{l_{av}} \quad (3)$$

where l_{av} is the average bond length, and l_i is the bond length between the B-site atom and the ith O atom. For an ideal cubic perovskite, D=0. Table 1 lists the bond lengths obtained in the crystal structural calculation from Figs. 6(c)-(d). After calculation, the distortion indices of Nb^{5+} in pure NN and Sn^{4+} atoms in $0.08Bi_{2/3}SnO_3$-$0.92NaNbO_3$ are 0.047 and 0.003, respectively. Therefore, the introduction of $Bi_{2/3}SnO_3$ can cause a decrease in the distortion index, presenting the same trend in the heating process. This reduction in octahedral distortion is likely the key factor enabling the retention of the high-temperature AFE R phase at RT, further supporting the phase transition mechanism.

Table 1 key bond lengths (Å) obtained in the structural calculation

B-O bond	Pure NN	$0.08Bi_{2/3}SnO_3$-$0.92NaNbO_3$
Nb/Sn-O32	2.005	2.063
Nb/Sn-O35	1.901	2.075
Nb/Sn-O38	2.179	2.062
Nb/Sn-O28	2.008	2.084
Nb/Sn-O43	2.159	2.067
Nb/Sn-O22	1.901	2.062
av	2.025	2.069

4 Conclusion

$x Bi_{2/3}SnO_3$-$(1-x)NaNbO_3$ ceramics were successfully fabricated via traditional solid state reactions. For compositions within $0.04 \leq x \leq 0.08$, samples exhibit reversible field-induced phase transitions ($E_{FE\text{-}AFE} > 0$) with a low operating field $E_{AFE\text{-}FE}$ below 200 $kV \cdot cm^{-1}$ and a remarkably low remanent polarization compared to other compositions. Our work demonstrates that achieving a low-field reversible phase transition in $NaNbO_3$ can be optimized by increasing the energy difference between

AFE and FE phases, enhancing the covalency of A-O and B-O bonds, reducing the distortion index, and introducing an appropriate level of dislocations.

Availability of data and materials

The data are available from the corresponding author upon reasonable request.

Competing interests

The authors have no competing interests to declare that are relevant to the content of this article.

Acknowledgements

This work was financed by the National Natural Science Foundation of China (52202141, 52172118) and Initiation Funds for High-level Talents Program of Xi'an International University (grant No. XAIU202519).

Electronic Supplementary Material (ESM)

Supplementary material is available in the online version of this article.

References

[1] Zhuo F, Li Q, Gao J, Wang Y, Yan Q, Xia Z, Zhang Y, Chu X. Structural phase transition, depolarization and enhanced pyroelectric properties of $(Pb_{1-1.5x}La_x)(Zr_{0.66}Sn_{0.23}Ti_{0.11})O_3$ solid solution. *J Mater Chem C* 2016, **4**: 7110-7118.

[2] Yang X, Zhuo F, Wang C, Liu Y, Wang Z, He C, Long X. Tunable pyroelectricity, depolarization temperature and energy harvesting density in $Pb(Lu_{0.5}Nb_{0.5})O_3$-$x$$PbTiO_3$ ceramics. *Acta Mater* 2020, **186**: 523-532.

[3] Liu Z, Lu T, Xue F, Nie H, Withers R, Studer A, Kremer F, Narayanan N, Dong X, Yu D, Chen L, Liu Y, Wang G. Lead-free (Ag,K)NbO_3 materials for high-performance explosive energy conversion. *Sci Adv* 2020, **6**: eaba0367.

[4] Yang B, Liu Y, Jiang R-J, Lan S, Liu S-Z, Zhou Z, Dou L, Zhang M, Huang H, Chen L-Q, Zhu Y-L, Zhang S, Ma X-L, Nan C-W, Lin Y-H. Enhanced energy storage in antiferroelectrics via antipolar frustration. *Nature* 2025, **637**: 1104-1110.

[5] Yang Z, Du H, Jin L, Poelman D. High-performance lead-free bulk ceramics for electrical energy storage applications: design strategies and challenges. *J Mater Chem A* 2021, **9**: 18026-18085.

[6] Zhuo F, Qiao H, Zhu J, Wang S, Bai Y, Mao X, Wu H-H. Perspective on antiferroelectrics for energy storage and conversion applications. *Chin Chem Lett* 2021, **32**: 2097-2107.

[7] Zhao P, Cai Z, Wu L, Zhu C, Li L, Wang X. Perspectives and challenges for lead-free energy-storage multilayer ceramic capacitors. *J Adv Ceram* 2021, **10**: 1153-1193.

[8] Berlincourt D. Transducers using forced transitions between ferroelectric and antiferroelectric states. *IEEE Trans Sonics Ultrason* 1966, **SU13**: 116-125.

[9] Uchino K. Digital displacement transducer using antiferroelectrics. *Jpn J Appl Phys* 1985, **24**: 460-462.

[10] Lin B, Ong KP, Yang T, Zeng Q, Hui HK, Ye Z, Sim C, Yen Z, Yang P, Dou Y, Li X, Gao X, Tan CKI, Lim ZS, Zeng S, Luo T, Xu J, Tong X, Li PWF, Ren M, Zeng K, Sun C, Ramakrishna S, Breese MBH, Boothroyd C, Lee C, Singh DJ, Lam YM, Liu H. Ultrahigh electromechanical response from competing ferroic orders. *Nature* 2024, **633**: 798-803.

[11] Zhang S-T, Kounga AB, Jo W, Jamin C, Seifert K, Granzow T, Rödel J, Damjanovic D. High-strain lead-free antiferroelectric electrostrictors. *Adv Mater* 2009, **21**: 4716-4720.

[12] Novak N, Weyland F, Patel S, Guo H, Tan X, Rödel J, Koruza J. Interplay of conventional with inverse electrocaloric response in (Pb,Nb)(Zr,Sn,Ti)O_3 antiferroelectric materials. *Phys Rev B* 2018, **97**: 094113.

[13] Mischenko AS, Zhang Q, Scott JF, Whatmore RW, Mathur ND. Giant electrocaloric effect in thin-film $PbZr_{0.95}Ti_{0.05}O_3$. *Science* 2006, **311**: 1270-1271.

[14] Vopson MM, Caruntu G, Tan X. Polarization reversal and memory effect in anti-ferroelectric materials. *Scripta Mater* 2017, **128**: 61-64.

[15] Zhang M-H, Hadaeghi N, Egert S, Ding H, Zhang H, Groszewicz PB, Buntkowsky G, Klein A, Koruza J. Design of lead-free antiferroelectric $(1-x)NaNbO_3$-$xSrSnO_3$ compositions guided by first-principles calculations. *Chem Mater* 2021, **33**: 266-274.

[16] Qi H, Xie A, Fu J, Zuo R. Emerging antiferroelectric phases with fascinating dielectric, polarization and strain response in $NaNbO_3$-$(Bi_{0.5}Na_{0.5})TiO_3$ lead-free binary system. *Acta Mater* 2021, **208**: 116710.

[17] Yang L, Kong X, Cheng Z, Zhang S. Enhanced energy storage performance of sodium niobate-based relaxor dielectrics by a ramp-to-spike sintering profile. *ACS Appl Mater Interfaces* 2020, **12**: 32834-32841.

[18] Egert S, Zhang M-H, Koruza J, Groszewicz PB, Buntkowsky G. ^{23}Na NMR spectroscopic quantification of the antiferroelectric-ferroelectric phase coexistence in sodium niobate. *The Journal of Physical Chemistry C* 2020, **124**: 23852-23858.

[19] Gouget G, Duttine M, Durand E, Villesuzanne A, Rodriguez V, Adamietz F, Le Mercier T, Braida M-D, Demourgues A. Isolating the two room-temperature polymorphs of $NaNbO_3$: structural features, optical band gap, and reactivity. *ACS Appl Electron Mater* 2019, **1**: 513-522.

[20] Dong X, Li X, Chen H, Dong Q, Wang J, Wang X, Pan Y, Chen X, Zhou H. Realizing enhanced energy storage and hardness performances in $0.90NaNbO_3$-$0.10Bi(Zn_{0.5}Sn_{0.5})O_3$ ceramics. *J Adv Ceram* 2022, **11**: 729-741.

[21] Dai S, Li M, Wu X, Wu Y, Li X, Hao Y, Luo B. Combinatorial optimization of perovskite-based ferroelectric ceramics for energy storage applications. *J Adv Ceram* 2024, **13**: 877-910.

[22] Peel MD, Thompson SP, Daoud-Aladine A, Ashbrook SE, Lightfoot P. New twists on the perovskite theme: crystal structures of the elusive phases R and S of $NaNbO_3$. *lnorg Chem* 2012, **51**: 6876-6889.

[23] Zhang M-H, Zhao C, Fulanović L, Rödel J, Novak N, Schökel A, Koruza J. Revealing the mechanism of electric-field-induced phase transition in antiferroelectric $NaNbO_3$ by in situ high-energy X-ray diffraction. *Appl Phys Lett* 2021, **118**: 132903.

[24] Shimizu H, Guo H, Reyes-Lillo SE, Mizuno Y, Rabe KM, Randall CA. Lead-free antiferroelectric: xCaZrO$_3$-(1-x)NaNbO$_3$ system (0</=x</=0.10). *Dalton Trans* 2015, **44**: 10763-10772.

[25] Zhang L, Pu Y, Chen M, Shi Y, Shang J, Yang Y, Zhao D. Novel (1-x)NaNbO$_3$-xBi$_{2/3}$HfO$_3$ based, lead-free compositions with stable antiferroelectric phase and high energy density and switching field. *Chem Eng J* 2023, **457**: 141376.

[26] Gao L, Guo H, Zhang S, Randall CA. A perovskite lead-free antiferroelectric xCaHfO$_3$-(1-x)NaNbO$_3$ with induced double hysteresis loops at room temperature. *J Appl Phys* 2016, **120**: 204102.

[27] Ye J, Wang G, Chen X, Cao F, Dong X. Enhanced antiferroelectricity and double hysteresis loop observed in lead-free (1-x)NaNbO$_3$-xCaSnO$_3$ ceramics. *Appl Phys Lett* 2019, **114**: 122901.

[28] Zhang M-H, Fulanović L, Zhao C, Koruza J. Review on field-induced phase transitions in lead-free $NaNbO_3$-based antiferroelectric perovskite oxides for energy storage. *J Materiomics* 2023, **9**: 1-18.

[29] Glazer AM, Megaw HD. Studies of the lattice parameters and domains in the phase transitions of $NaNbO_3$. *Acta Crystallogr, Sect A:Found Crystallogr* 1973, **29**: 489-495.

[30] Tian A, Zuo R, Qi H, Shi M. Giant energy-storage density in transition-metal oxide modified $NaNbO_3$-Bi($Mg_{0.5}Ti_{0.5}$)O_3 lead-free ceramics through regulating antiferroelectric phase structure. *J Mater Chem A* 2020, **8**: 8352-8359.

[31] Xie A, Qi H, Zuo R, Tian A, Chen J, Zhang S. An environmentally-benign $NaNbO_3$ based perovskite antiferroelectric alternative to traditional lead-based counterparts. *J Mater Chem C* 2019, **7**: 15153-15161.

[32] Chen M, Pu Y, Zhang L, Yang Y, Wang B, Shang J. Phase transition, antiferroelectric and pulse discharge properties of $(1-x)NaNbO_3$–$xBi_{2/3}ZrO_3$ ceramics. *Ceram Int* 2024, **50**: 52096-52102.

[33] Chen M, Pu Y, Ding H, Zhang L, Xu N, Kleebe H-J, Molina-Luna L. Phase identification and structural evolution in BMT modified NN anti-ferroelectric ceramics. *J Eur Ceram Soc* 2022, **42**: 6504-6511.

[34] Qi H, Zuo R, Xie A, Tian A, Fu J, Zhang Y, Zhang S. Ultrahigh energy‐storage density in $NaNbO_3$‐based lead‐free relaxor antiferroelectric ceramics with nanoscale domains. *Adv Funct Mater* 2019, **29**: 1903877.

[35] Ma T-C, Xu B, Zheng M, Hou Y, Wang K, Gong W, Zhang M-H. Revealing the role of B-site cations in the antiferroelectricity of $NaNbO_3$-based perovskites. *J Eur Ceram Soc* 2025, **45**: 116928.

[36] Chao W, Yang T, Li Y. Achieving high energy efficiency and energy density in $PbHfO_3$-based antiferroelectric ceramics. *J Mater Chem C* 2020, **8**: 17016-17024.

[37] Kresse G, Furthmüller J. Efficient iterative schemes for ab initio total-energy calculations using a plane-wave basis set. *Phys Rev B: Condens Matter* 1996, **54**: 1169-11186.

[38] Perdew JP, Burke K, Ernzerhof M. Generalized gradient approximation made simple. *Phys Rev Lett* 1996, **77**: 3865-3868.

[39] Langreth DC, Mehl M. Beyond the local-density approximation in calculations of ground-state electronic properties. *Phys Rev B* 1983, **28**: 1809-1834.

[40] Monkhorst HJ, Pack JD. Special points for Brillouin-zone integrations. *Phys Rev B* 1976, **13**: 5188.

[41] Ma J, Zhang J, Guo J, Li X, Guo S, Huan Y, Wang J, Zhang S-T, Wang Y. Achieving Ultrahigh Energy Storage Density in Lead-Free Sodium Niobate-Based Ceramics by Modulating the Antiferroelectric Phase. *Chem Mater* 2022, **34**: 7313-7322.

[42] Dong X, Li X, Chen X, Tan Z, Wu J, Zhu J, Zhou H. (1-x)[0.90NN-0.10Bi($Mg_{2/3}Nb_{1/3}$)O_3]-x($Bi_{0.5}Na_{0.5}$)$_{0.7}Sr_{0.3}TiO_3$ ceramics with core–shell structures: A pathway for simultaneously achieving high polarization and breakdown strength. *Nano Energy* 2022, **101**: 107577.

[43] Zhang M-H, Fulanović L, Egert S, Ding H, Groszewicz PB, Kleebe H-J, Molina-Luna L, Koruza J. Electric-field-induced antiferroelectric to ferroelectric phase transition in polycrystalline $NaNbO_3$. *Acta Mater* 2020, **200**: 127-135.

[44] Xie A, Fu J, Zuo R. Achieving stable relaxor antiferroelectric P phase in $NaNbO_3$-based lead-free ceramics for energy-storage applications. *J Materiomics* 2021, **8**: 618-626.

[45] Qiao Z, Li T, Qi H, Zuo R. Excellent energy storage properties in $NaNbO_3$-based lead-free ceramics by modulating antiferrodistortive of P phase. *J Alloys Compd* 2022, **898**: 162934.

[46] Chen J, Qi H, Zuo R. Realizing stable relaxor antiferroelectric and superior energy storage properties in ($Na_{1-x/2}La_{x/2}$)($Nb_{1-x}Ti_x$)O_3 lead-free ceramics through A/B-site complex substitution. *ACS Appl Mater Interfaces* 2020, **12**: 32871-32879.

[47] Xie A, Fu J, Zuo R, Zhou C, Qiao Z, Li T, Zhang S. $NaNbO_3$-$CaTiO_3$ lead-free relaxor antiferroelectric ceramics featuring giant energy density, high energy efficiency and power density. *Chem Eng J* 2022, **429**: 132534.

[48] Shen ZX, Wang XB, Kuok MH, Tang SH. Raman scattering investigations of the antiferroelectric–ferroelectric phase transition of $NaNbO_3$. *J Raman Spectrosc* 1998, **29**: 379-384.

[49] Lin SJ, Chiang DP, Chen YF, Peng CH, Liu HT, Mei JK, Tse WS, Tsai T-R, Chiang H-P. Raman scattering investigations of the low-temperature phase transition of $NaNbO_3$. *J Raman Spectrosc* 2006, **37**: 1442-1446.

[50] Mishra KK, Sivasubramanian V, Arora AK. Low-temperature Raman spectroscopic studies in $NaNbO_3$. *J Raman Spectrosc* 2011, **42**: 517-521.

[51] Yuzyuk YI, Gagarina E, Simon P, Reznitchenko LA, Hennet L, Thiaudie`re D. Synchrotron X-ray diffraction and Raman scattering investigations of $(Li_xNa_{1-x})NbO_3$ solid solutions: evidence of the rhombohedral phase. *Phys Rev B* 2004, **69**: 144105.

[52] Shiratori Y, Magrez A, Dornseiffer J, Haegel F-H, Pithan C, Waser R. Polymorphism in micro-, submicro-, and nanocrystalline $NaNbO_3$. *The Journal of Physical chemistry B* 2005, **109**: 20122-20130.

[53] Wang XB, Shen ZX, Hu ZP, Qin L, Tang SH, Kuok MH. High temperature Raman study of phase transitions in antiferroelectric $NaNbO_3$. *J Mol Struct* 1996, **385**: 1-6.

[54] Megaw HD. The seven phases of sodium niobate. *Ferroelectrics* 1974, **7**: 87-89.

[55] Wu J, Liu H, Qi H, Gao B, Chen L, Li W, Deng S, Chen J. Stabilization of the ferrielectric phase in $NaNbO_3$-based lead-free ceramics for a wide-temperature large electrocaloric effect. *J Mater Chem A* 2022, **10**: 18070-18077.

[56] Ye J, Wang G, Chen X, Dong X. Effect of rare-earth doping on the dielectric property and polarization behavior of antiferroelectric sodium niobate-based ceramics. *J Materiomics* 2021, **7**: 339-346.

[57] Uchino K, Nomura S. Critical exponents of the dielectric constants in diffused-phase-transition crystals. *Ferroelectrics* 2011, **44**: 55-61.

[58] Shvartsman VV, Lupascu DC, Green DJ. Lead-free relaxor ferroelectrics. *J Am Ceram Soc* 2012, **95**: 1-26.

[59] Li S, Hu T, Nie H, Fu Z, Xu C, Xu F, Wang G, Dong X. Giant energy density and high efficiency achieved in silver niobate-based lead-free antiferroelectric ceramic capacitors via domain engineering. *Energy Storage Mater* 2021, **34**: 417-426.

[60] Dong X, Li X, Chen X, Chen H, Sun C, Shi J, Pang F, Zhou H. High energy storage and ultrafast discharge in $NaNbO_3$-based lead-free dielectric capacitors via a relaxor strategy. *Ceram Int* 2021, **47**: 3079-3088.

[61] Gupta VV, Mansingh A. Hopping conduction in insulating rf-sputtered zinc oxide films. *Phys Rev B: Condens Matter* 1994, **49**: 1989-1995.

[62] Zhang L, Pu Y, Chen M. Complex impedance spectroscopy for capacitive energy-storage ceramics: a review and prospects. *Mater Today Chem* 2023, **28**: 101353.

[63] Ma L, Che Z, Luo Y, Xu C, Cen Z, Toyohisa F, Zhang S, Li J-F, Luo N. Record-breaking electrostrain in NaNbO3-based antiferroelectric ceramics via achieving fully reversible phase transition. *Acta Mater* 2025, **289**: 120950.

[64] Chen J, Pen D. TEM study of phases and domains in $NaNbO_3$ at room temperature. *Phys Status Solidi* 1988, **109**: 171-185.

[65] Hu T, Fu Z, Zhang L, Ye J, Chen X, Wang G, Xu F. Spatial buffer-area assisted antiferroelectric-ferroelectric transition in $NaNbO_3$. *Scripta Mater* 2023, **227**: 115295.

[66] Li N, Zhu R, Cheng X, Liu H-J, Zhang Z, Huang Y-L, Chu Y-H, Chen L-Q, Ikuhara Y, Gao P. Dislocation-induced large local polarization inhomogeneity of ferroelectric materials. *Scripta Mater* 2021, **194**: 113624.

[67] Gao P, Nelson CT, Jokisaari JR, Baek SH, Bark CW, Zhang Y, Wang E, Schlom DG, Eom CB, Pan X. Revealing the role of defects in ferroelectric switching with atomic resolution. *Nat Commun* 2011, **2**: 591.

[68] Jiang T, Ni F, Recalde-Benitez O, Breckner P, Molina-Luna L, Zhuo F, Rödel J. Observation of dislocation-controlled domain nucleation and domain-wall pinning in single-crystal $BaTiO_3$. *Appl Phys Lett* 2023, **123**: 202901.

[69] Zhuo F, Wang B, Cheng L, Zatterin E, Jiang T, Ni F, Breckner P, Li Y, Guiblin N, Isaia D, Luo N, Fulanovic L, Molina-Luna L, Dkhil B, Chen L-Q, Rödel J. Unlocking Electrostrain in Plastically Deformed Barium Titanate. *Adv Mater* 2024, **36**: 2413713.

[70] Becke AD, Edgecombe KE. A simple measure of electron localization in atomic and molecular systems. *The Journal of Chemical Physics* 1990, **92**: 5397-5403.

[71] Xu M, Cheng YQ, Sheng HW, Ma E. Nature of atomic bonding and atomic structure in the phase-change $Ge_2Sb_2Te_5$ glass. *Phys Rev Lett* 2009, **103**: 195502.

[72] Silvi B, Savin A. Classification of chemical bonds based on topological analysis of electron localization functions. *Nature* 1994, **371**: 683-686.

[73] Levin I, Krayzman V, Woicik JC, Karapetrova J, Proffen T, Tucker MG, Reaney IM. Structural changes underlying the diffuse dielectric response in $AgNbO_3$. *Phys Rev B* 2009, **79**: 104113.

[74] Baur WH. The geometry of polyhedral distortions. predictive relationships for the phosphate group. *Acta Crystallogr Sec B* 1974, **30**: 1195-1215.